SCIENCE CHINA
Technological Sciences

•Article•

August 2019 Vol.62 No.8: 1401–1411
https://doi.org/10.1007/s11431-018-9408-3

Variable-model SMA-driven spherical robot

PAN Jie, SHI ZhenYun* & WANG TianMiao

Robotic Laboratory, Beihang University, Beijing 100191, China

Received July 5, 2018; accepted December 10, 2018; published online July 19, 2019

In this paper, we introduce a bionic spherical robot. This research has been inspired by the muscular organs and modularity of organisms such as starfish and octopuses. The robot that we fabricated uses five soft feet to crawl like a starfish, and the robotic feet are driven by the shape memory alloy springs. The robotic spherical structure and the soft feet were fabricated by 3D printing. The robotic feet were made of silicone gel; these feet could bend upward and downward to help the robot to crawl on the ground and roll down a slope. The shell separation module installed inside the robot could divide the robot into two identical modules, and this smart structure could enhance the robotic flexibility in a small space. We performed force analysis and robotic simulation, and the results verified the feasibility of the model. The robot can switch between rigidity and softness by using human control. Three types of gaits have been proposed for controlling robotic movement and improving robotic flexibility in movement; these include rolling, crawling, and avoiding obstacles. The results of this study indicate that the variable-model design of the robot is an effective way to enhance the flexibility of soft robots.

bionic, robot, soft animals, shape memory alloy, smart structure, variable model

Citation: Pan J, Shi Z Y, Wang T M. Variable-model SMA-driven spherical robot. Sci China Tech Sci, 2019, 62: 1401–1411, https://doi.org/10.1007/s11431-018-9408-3

1 Introduction

In recent years, biomimetic technology has been widely applied to robots [1]. Soft robot technology is a novel technology in the field of robotics, and a number of studies have been performed in this field [2]. Soft robots are made of soft materials and are more flexible than traditional rigid robots [3,4]. The bodies of soft robots can generate large deformations [5], and their performance is superior to rigid robots in some special instances. A soft robot can enter into tight spaces and change their shapes to adapt to the surrounding environment; they can also crawl smoothly and move fragile objects safely [6]. The softness of the robot makes it possible to continue working by using the driving force even when their bodies are impacted by outside collisions [7,8]. At present, there are three main areas for soft robot researches [9–12]. The first area includes traditional wire-driven and pneumatic research, such as the trunk robot developed by the German company Festo [13], and the relatively mature pneumatic muscle [14]. The second area is the pneumatic robotic technology, mainly led by Harvard University. Currently, this area is a research hotspot for soft robots. Researchers in this area use the 3D printing technology to fabricate the body of a robot based on the elastic material [9]. The robots have the advantage of flexible movement, large deformation, and small sizes. The third research area uses techniques based on smart materials, such as the shape memory alloys (SMAs) [15,16], shape memory polymers [17,18], and electroactive polymers [19–21]; robots made from smart materials have a number of advantages, such as small size and stable motion.

However, it is difficult to fabricate and control soft robots [22]. Soft robots are mostly made of elastic materials (e.g., silicone gel); therefore, these robots have more freedom because they are less rigid. However, theoretical modeling and motion control for soft robots is more difficult than those

*Corresponding author (email: shichong1983623@hotmail.com)

for rigid robots [10,23,24]. Although soft robots can achieve basic movements, their load capacity is weak. Moreover, soft robots move slowly and their accuracy control is difficult [25,26]. To date, the bodies of most soft robots are flexible with relatively simple forms of motion. Soft robots have slow motion speeds, and the softness of its body makes the sensor devices and the control chips difficult to mount on the body. Therefore, it is important to find ways of improving the mobility and the load-carrying capacity of soft robots [27].

To overcome the existing problems of soft robots, we designed a type of soft spherical robot. According to the environment, this robot can function in two modes: "rigid" or "flexible" through human control. This robot can also achieve some behaviors, such as crawling, rolling, and the separation of the spherical shell; these characteristics have not been reported in the field of soft robots. SMA springs [28,29] were used as robotic drivers, and silicone gel was applied to fabricate the robotic feet. In this study, the complicated spherical shell was fabricated by using 3D printing technology [30].

2 Robot fabrication

2.1 Shapes of the robot

In nature, a starfish has soft and flexible limbs that move at low speeds, and they have particularly smooth movements. A starfish has five soft limbs (Figure 1(a)); these limbs are flexible and allow the starfish to move forward and backward and avoid obstacles by the coordinated movement of these limbs [31]. Although soft limbs make the starfish flexible, these limbs also make the starfish slow. To improve speed, we designed a spherical robot that combined the crawling motion of a starfish and the rolling motion of a sphere. A starfish is a marine echinoderm, and its feet are made of muscles and tendons. The foot flexes upward when the tendon near the epidermis contracts, and the foot flexes downward when the tendon near the lower epidermis contracts. Inspired by the foot structure of a starfish, we used silicone gel for the soft robot's foot muscles, and the SMA springs were used as internal tendons. Figure 1(c) shows that the robotic feet are independently mounted on the spherical shell; these feet were made modular instead of integral. This special structure enabled us to replace the silicone gel feet easily and avoid material waste when the robotic structures were damaged.

The robotic external structure consists of two hemispherical shells with ten silicone gel feet. In a fully closed state, the spherical robot's foot becomes spherical, as shown in Figure 1(d). In this state, the robot is rigid and can quickly roll down a slope. When the robot crawls on the ground, the robot is in a soft state, and the five robotic silicone gel feet under the ball move sequentially using a special gait.

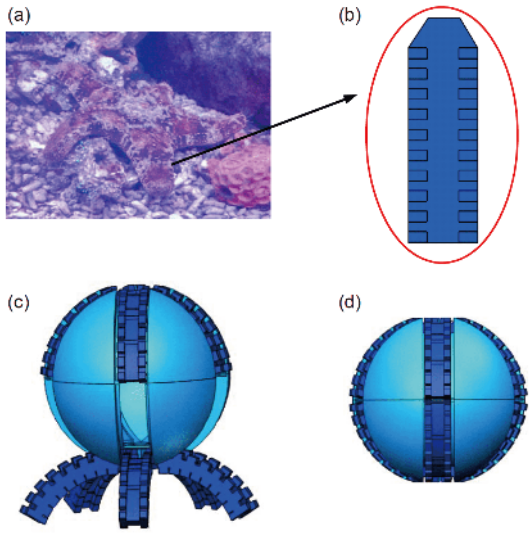

Figure 1 (Color online) (a) Starfish shape; (b) robotic foot; (c) crawling by the robot; (d) spherical shape.

2.2 Robot shell design

To reduce the weight of the shell and the difficulty involved in making the curved robotic shell, the shell of the robot was manufactured using 3D printing technology. In addition, for the shell material, we used a light resin with high rigidity. The spherical shell was made into two hemispherical shells constrained by electromagnets in the shell. The hemispherical shell contained five fan-shaped structures to limit the bending range of the foot. The thickness of the shell was 2 mm, and the five notches were evenly arranged in the circumferential direction of the shell to restrain the soft leg. The shell was impacted from the outside during the rolling, therefore, it was necessary to arrange a plank inside the shell to make the shell more secure, the plank was depicted in Figure 2(c). In particular, the spherical shell could be divided into two independent hemispherical modules, and the two modules could move independently. If the robot needed to enter a small space while moving or needed to simultaneously detect two directions, the separation of the spherical shell could easily help.

2.3 Foot design

The surface muscles of starfish and octopuses have wedge-shaped structures instead of smooth structures. Such special structures help reduce the tensile stresses generated by the muscles on the skin surface during muscle contraction; these structures can also support the flexible extension of organs.

Inspired by biological organs, we designed a wedge-shaped structure for the robotic feet. This special structure includes three common wedge-shaped corner structures with different mechanical properties. To select a suitable wedge-shaped structure, we performed simulation experiments on

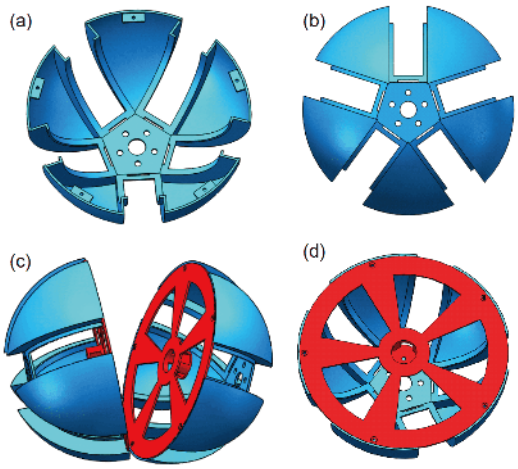

Figure 2 (Color online) Design of the spherical shell. (a) Top view of the shell; (b) bottom display of the shell; (c) separation of the robot; (d) constraint of the shell.

these models. In the simulation, the material properties were taken to be the same as Skin 881 (Duocaihani Inc., Shenzhen, China). The silicone rubber elastic modulus value was set to 2.14 MPa; the Poisson's ratio was 0.49, and the density was 1.4 g/cm^3. The grid structure was the tetrahedron in the simulation software Abaqus (Abaqus 6.13, SIMULIA Inc., France). The model was set as a variable body with a time step of 1 s, and the geometric nonlinear analysis was turned on; the solver type was explicit dynamic. After the simulation, the three structures exhibited different mechanical flexing properties, as shown in Figure 3(a). As it was difficult to design the silicone mold and the soft foot, therefore we chose a 90° wedge-angle structure. The SMA springs generated heat when they were energized; therefore, we needed to consider the heat dissipation. Grooves were designed on both sides of the feet to constrain the SMA springs; this not only increased the area of contact between the feet and the ground, but they also helped cool down the SMA springs quickly. To keep the SMA spring in an effective position when under stress, we designed polyether ether ketone (PEEK) material baffles to constrain the SMA springs. The PEEK planks were light and able to withstand the SMA temperature; these planks were arranged sequentially in the foot space, as shown in Figure 3(c).

2.4 SMA spring selection

The initial length L_0 of the spring was 30 mm (The spring was produced by GEE Inc. from Beijing and was based on nickel titanium; it had a one-way memory effect with a transition temperature of 69°C. The spring had diameters of 4.6 and 4.8 mm, and the wire diameters were 0.7 and 0.8 mm). As shown in Figure 4, the spring was mounted on a laser displacement sensor platform, and its tensile length was marked. To control the heating rate of the SMA spring and avoid fatigue damage, the SMA was driven by pulse width modulation. The SMA spring resistance value was measured as 2 Ω, at room temperature by using the experimental test. The heating time referred to the time for which the SMA spring was energized. The shrinking was more stable when the heating cycle T of the SMA spring was less, and the impedance effect was high. The maximum operating frequency of the spring was 0.5 Hz, and the minimum heating

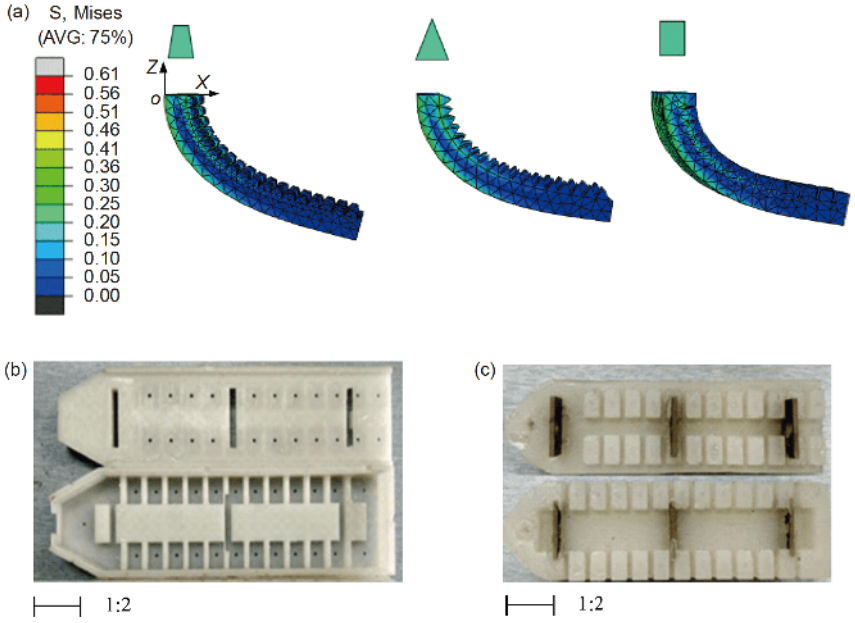

Figure 3 (Color online) Design and fabrication of the foot. (a) Bending result of the three wedge-shaped feet under the same condition; (b) the mold; (c) the silicone foot.

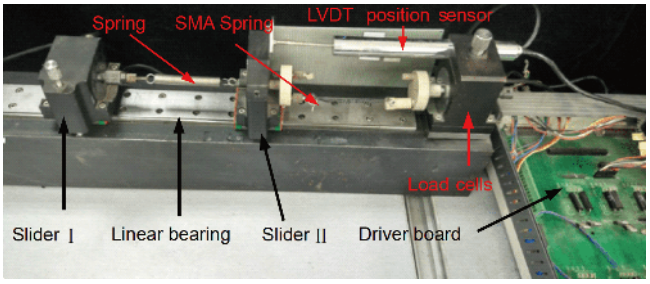

Figure 4 (Color online) Experimental platform for SMA springs.

period of the spring was 2 s. To avoid too much heating of the spring and to control the actuating rate effectively during the heating time, we set the duty cycle to 85%.

We measured the force of the SMA spring by using a tension sensor (PUYAN Inc., China); the measuring error was 0.1 N. Figure 5 shows that the SMA spring was pre-heated for the first 8 s, which indicated that the spring exerted a hysteresis effect of approximately 8 s in the experiment. After 8 s, the SMA spring's force rose rapidly and reached a maximum; then, its temperature decreased slowly. The curve did not return to the initial point because of the thermal stress inside the spring. It is possible to show that the different deformation of the SMA springs can generate different shrinking force.

From the above analysis, the approximate length of the SMA springs and the heating time can be determined. We assumed that the longitudinal load P of the SMA spring was resisted by the shear stress on the coil spring wire portion, and the spring was subjected to a uniform torque, its shear force varied linearly along the radius. Thus, the maximum shear force $\tau_{\max}$ on the spring wire caused by the load P is

$$\tau_{\max} = k\frac{8PD}{\pi d^3}, \tag{1}$$

where the stress correction factor k is defined by the Wahl stress correction formula as follows:

$$k = \frac{4C-1}{4C-4} + \frac{0.615}{C}, \tag{2}$$

where the C is the spring index. The spring tension σ caused by the load P is

$$\sigma = \frac{8PD^3N}{Gd^4}. \tag{3}$$

When the soft foot bends upward, the spring length is given by δ_0. When the soft foot was parallel to the horizontal line, the spring length was δ_1. The displacement δ is defined as

$$\delta = \delta_1 - \delta_0. \tag{4}$$

Thus, the number of turns of the SMA spring is given as

$$N = \frac{(\delta_1-\delta_0)d}{\pi\tau_s D^2}, \tag{5}$$

where τ_s is the shear strain difference of the SMA spring in a high- and low-temperature phase-change environment.

The length of the SMA spring was set as 30 mm. When the spring was stretched to 90 mm, it could provide a shrinking force of 12 N during heating. Based on the above analysis, we can calculate the number of turns of the SMA spring.

3 Movement mechanism

3.1 Analysis of the foot

The SMA springs were distributed on both sides of the soft foot. The upper spring needed to overcome gravity during bending; therefore, analyzing the upward bending was enough to evaluate the mechanical properties of the foot. When we energized the upper part of the soft spring and stretched the lower spring of the foot, we found that the soft foot flexed under the bending moment of the upper spring. The effective part of the foot is the green area shown in Figure 6(a); therefore, the stress analysis on the SMA spring and the foot can be simplified as shown in Figure 6(b). The contraction force of the spring changes nonlinearly during the SMA spring's phase changes (Figure 6(b)), and the elastic modulus is not the same as in the high- and low-temperature states. To

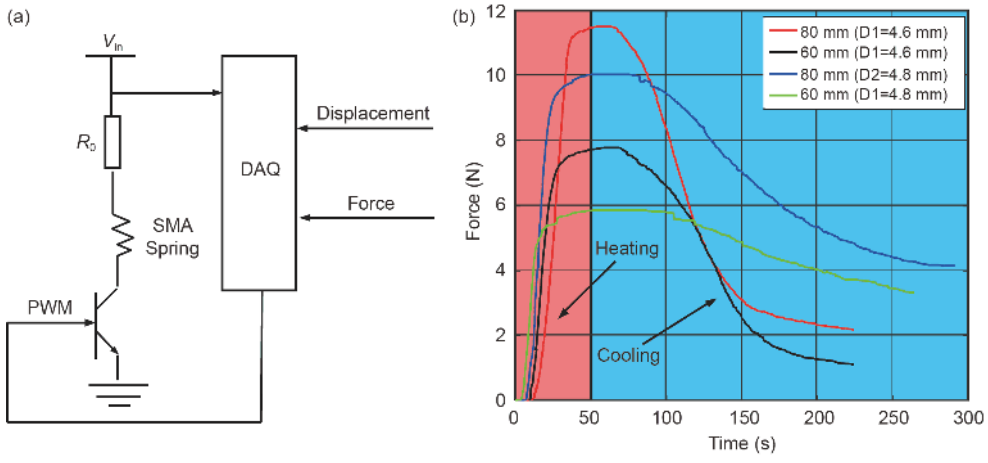

Figure 5 (Color online) (a) Heating strategy for the SMA spring; (b) forces generated by SMA springs at different deformation rates during energizing.

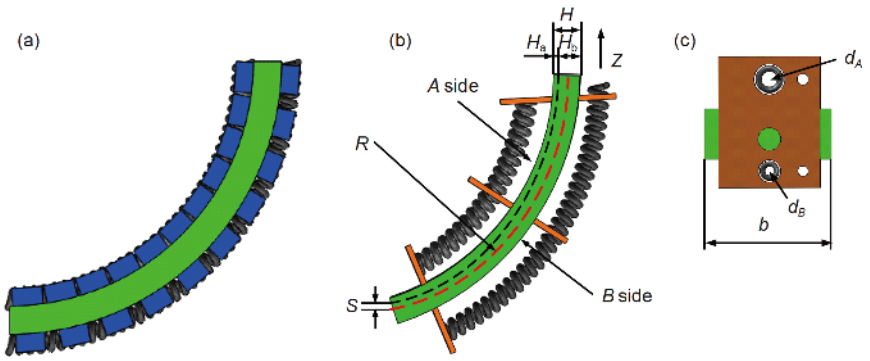

Figure 6 Structure of the foot. (a) Shape of the foot; (b) parameters of the effective parts; (c) parameters of the cross section.

calculate the SMA spring force as a function of time, the data obtained from the experiment were calculated using the Gaussian function in Matlab (Matlab 2010-a, MathWorks Inc., USA), and the data were fitted using the quintic polynomial expressed by the following relationship:

$$P = \sum_{i=1}^{5} a_{\mathrm{i}} \cdot e^{-((T-b_i)^2/c_i)^2}, \tag{6}$$

where a, b, and c are coefficients, which can be calculated by the experimental data.

To facilitate the analysis of the robot model, the maximum force of the spring was used as a constant force for the deformation of the foot. The B side SMA spring can use the gravity of silicone and the spring to bend, but the SMA spring of the A side has to overcome gravity. Thus, the A surface spring needs to be selected suitably because it need produce a large force to drive the foot. If the mass of the *PEEK* baffles could be ignored, the axial force balance equation is

$$\int_T Ek_1 bz\mathrm{d}z + P_{\mathrm{SMA\_}A} + P_{\mathrm{SMA\_}B} + mg = 0, \tag{7}$$

where E (Pa) is the elastic modulus of the foot; k is the foot curvature while bending; b is the width of the soft foot; $P_{\mathrm{SMA\_}A}$ is the tensile force of the SMA spring on the A side; $P_{\mathrm{SMA\_}B}$ is the contraction force of the SMA spring on the B side; m is the weight of the foot; and g is the gravitational acceleration.

$$\varepsilon = 8n_{\mathrm{s}}\pi PC^3 k\left(\frac{1}{G_{\mathrm{L}}} - \frac{1}{G_{\mathrm{H}}}\right), \tag{8}$$

$$C = \frac{D_B}{d_B}, \tag{9}$$

where C is the index of SMA spring; ε is the spring contraction of the side of A; D_B is the diameter of the spring; d is the diameter of the spring wire on the surface B; n is the number of turns of the spring; G_{H} is the modulus of elasticity of the SMA spring at high temperatures; and G_{L} is the elasticity modulus of the SMA spring at room temperature.

The bending moment of the foot balance equation is

$$P_{\mathrm{SMA\_}A}\left(H_{\mathrm{a}} + \frac{D_B}{2}\right) - \int_T Ek_1 bz^2\mathrm{d}z - P_{\mathrm{SMA\_}B}\left(H_{\mathrm{b}} + \frac{D_B}{2} + s\right) - \frac{mg}{2}(L - R\theta + 2R\cos\theta/2)\cos\theta/2 = 0, \tag{10}$$

where H_{a} is the upper thickness of the foot relative to the geometric middle layer; H_{b} is the lower thickness of the foot of the geometric middle layer; L is the length of the foot; s is the offset of the middle layer relative to the geometric middle layer during foot bending.

To facilitate the analysis, the bending line of the foot was defined as the standard arc. The radius of the arc is R, and the relationship between the bending angle θ and the spring strain $\varepsilon_{\mathrm{SMA}}$ in the bending process of foot is as follows:

$$\theta = \frac{(1-\varepsilon_{\mathrm{SMA\_}B})}{(R - s - \frac{H_a + H_b + D_B}{2})} L_{\mathrm{SMA\_}B} = \frac{(1+\varepsilon_{\mathrm{SMA\_}A})}{(R - s + \frac{H_a + H_b + D_B}{2})} L_{\mathrm{SMA\_}A}, \tag{11}$$

where $L_{\mathrm{SMA\_}A}$ and $L_{\mathrm{SMA\_}B}$ are the initial lengths of the A-side and B-side of the SMA spring, respectively, and $\varepsilon_{\mathrm{SMA\_}A}$ and $\varepsilon_{\mathrm{SMA\_}B}$ are the shrinkage strains of the A-plane spring and the B-plane spring, respectively.

By ignoring the micro deformation of silica gel, we obtain the following relationship from eqs. (9)–(11):

$$P_{\mathrm{SMA\_}A} = \frac{\int_T Ek_1 bz^2\mathrm{d}z + P_{\mathrm{SMA\_}B}(H_{\mathrm{b}} + D_B/2 + s) + \frac{mg}{2}(L - R\theta + 2R\cos\theta/2)\cos\theta/2}{(H_{\mathrm{a}} + D_B/2)}. \tag{12}$$

From Table 1, we can obtain that when θ is $\pi/2$, the value of $P_{\mathrm{SMA\_}A}$ is 5 N, which is less than the SMA spring's maximum force of 12 N. The above theoretical calculations show that the soft foot can achieve a bending of $\pi/2$ when driven by

Table 1 Numerical values of the parameters in the thermal dynamic model

Parameter	m	A	c	A_w	R	U	T_1
Value	1.47 g	500×10^{-6} mm	1000 (J/(kg K))	20 (W/(m^2 °C))	2 Ω	3.8 V	28.5°C

the SMA spring.

3.2 Heating times of SMA springs

The SMA spring can generate a shrinking force because of the temperature changes in the phase of the SMA material [15]. If the temperature of the spring is continuously increased during heating time, the SMA performance will deteriorate. Therefore, it is necessary to study the relationship between the heating time and the temperature of the SMA spring. The resistor value R of the SMA spring and the surface thermal conductivity h_w can be regarded as constants if the phase transition process is neglected. Therefore, the temperature changes can be expressed as follows:

$$U^2/R - mcdT/dt = -h_wA(T - T_1). \tag{13}$$

Base on eq. (13), we can obtain the following relationship between the temperature T of the SMA and the heating time t:

$$T = W \cdot e^{th_wA/(mc)} - U^2/(Rh_wA) + T_1, \tag{14}$$

where W is a constant; U is the voltage; R is the resistance of one SMA spring that is obtained from the experiment; A is the heating area; m is the mass of one SMA spring; T_1 is the temperature of the environment; h_w is the coefficient of heating conduction; c is the specific heat capacity of the SMA springs; and t is the heating time of the SMA spring.

Thus we can obtain the changing progressing of temperature while the SMA spring was heated in simulation, the result is shown in Figure 7.

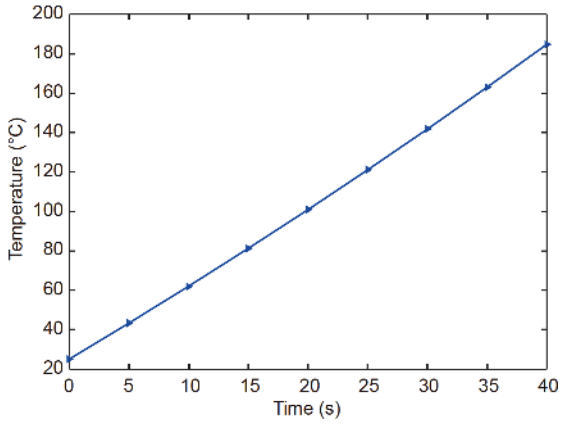

Figure 7 (Color online) The relationship between the heating time and temperature.

3.3 Design of the crawling gait

The spring temperature increases continuously while being energized because of the resistance of the SMA spring. The temperature changes are shown in Figure 8(a). If the heating time is too long, the working time of the spring will decrease. Figure 8(b) shows that the rate of upward bending of the foot is greater than the rate of downward bending, which is caused by the weight of the shell and the foot. Therefore, we need to set different heating times for the springs on both sides. The relationship between the foot's bending angle and the SMA's heating time was investigated using a thermocouple (K-type, 1.5 mm diameter, 200 mm long, Feiyang electro thermal Inc., China). As shown in Figures 7 and 8(a), the temperature trends are not exactly the same. This phenomenon can be interpreted as the specific heat capacity of the SMA material; this value changes with temperature. Human error is also one of the important factors in the measurement process. The thickness of the heat-conducting silicone grease in the experiment, and the airflow around the test bench affected the experimental results. There was an error of about 1°C in the temperature measurement experiment.

SMA springs can drive the feet to bend and establish robotic motion; therefore, the design of the crawling gaits and a reasonable control strategy are the key factors to improve the flexibility of a robot. Figure 9(a) and (b) shows two types of crawling gaits. Blue color specifies that the foot is relaxed, and red color specifies that the foot is driven by a downward bending force. Pink color specifies that there is an upward bending force. Figure 9(c) and (d) shows the heating strategies of SMA springs on the lower side of the foot. The high level means that the SMA spring is energized, whereas the low level means that the power is switched off. Here, we use Gait 1 as an example by dividing this gait into five parts. In the beginning, all five feet of the robot were on the ground, and the center of gravity of the robot dropped to the lowest. In the second step, the robotic feet A-B started bending toward the ground, and the ground generated a forward friction to drive the foot. Then, the robotic center of gravity began to move forward. In the third step, the robotic feet C-D bent down, and the robot could almost stand up completely. In the fourth step, the robotic foot E bent downward and accumulated the elastic potential energy. In the fifth step, the A and B feet bent upwards, and the center of gravity of the robot moved forward again and finally returned to its original height.

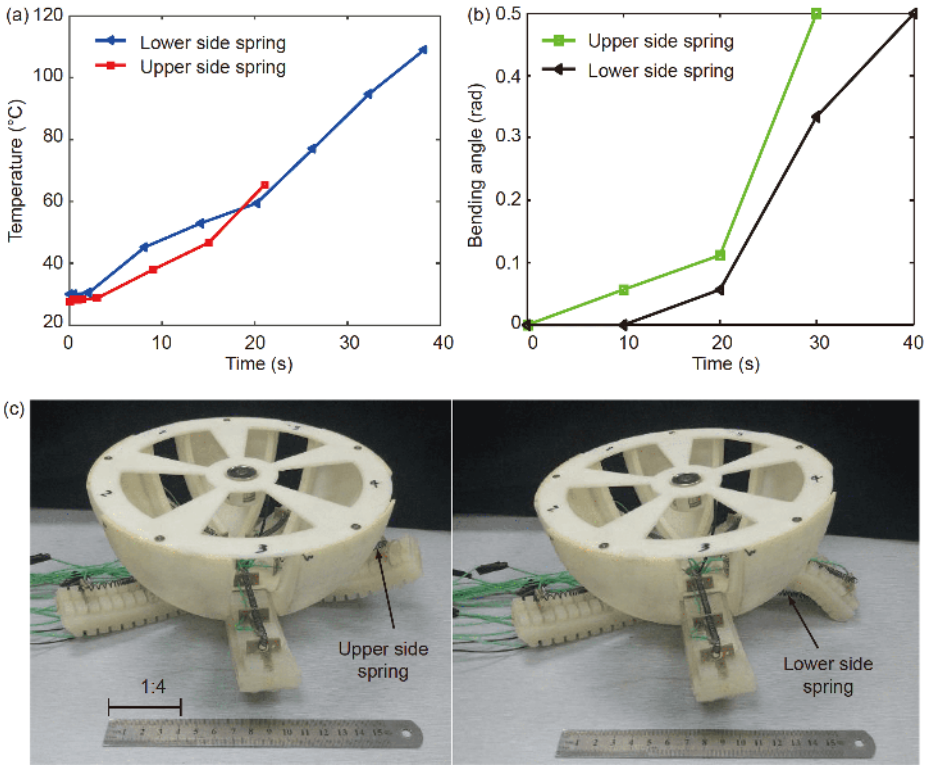

Figure 8 Heating the SMA spring of the foot. (a) Temperature of the upper side and lower side springs; (b) bending range when the foot bends up and down; (c) position of the SMA spring on the foot.

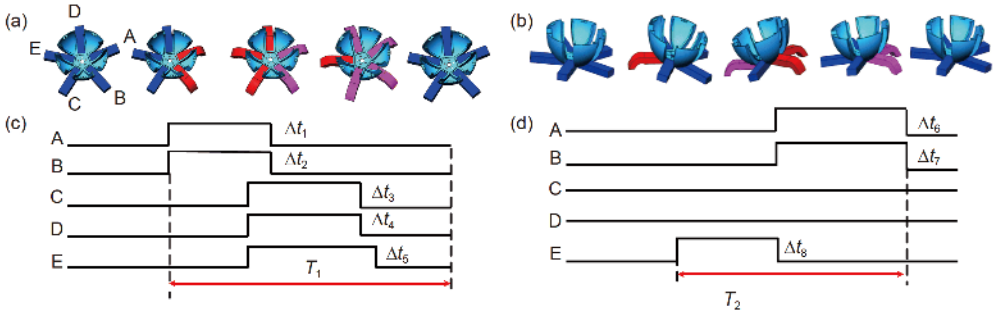

Figure 9 Heating strategy for the SMA springs. (a) Gait 1 diagram; (b) Gait 2 diagram; (c) heating strategy for Gait 1; (d) heating strategy for Gait 2.

4 Results and discussion

4.1 Simulation and experiment of foot bending

Based on eq. (6), the relationship between the heating time t and the force F is as follows:

$$F = 6.477 \cdot e^{-((t-50.84)/18.89)^2} + 7.488 \cdot e^{-((t-77.25)/29.9)^2} + \cdots + 2.376 \cdot e^{-((t-193.8)/80.66)^2}. \quad (15)$$

The force F applied on the foot in the simulation depends on the heating time of the SMA spring. In the simulation environment, the model was set as a variable body with a time step of 30 s, and geometric nonlinear analysis was turned on. The mesh type of the model is a tetrahedron, and the number of meshes was calculated by using Abaqus. The solver type was explicitly dynamic and did not include the thermodynamic analysis. As shown in Figure 10(a) and (b), the foot model could bend to a predetermined angle with the force F. These results prove the correctness of the SMA spring and the foot model.

Figure 10 shows that the foot-bending angle is different when the heating time is different. The reasons are: (1) The properties of the samples made in the mold were not completely identical to the material properties defined in the simulation software; therefore, experimental error was unavoidable; (2) The cooling rate of the SMA spring during heating was easily affected by the environment, such as the variable flow.

We concluded that accurately testing SMA in closed en-

vironments could reduce experimental errors. Reducing the SMA spring's preheating time is an effective way to improve the robotic working speed in the future.

4.2 Result of crawling

As shown in Figure 11(b), the robotic moving range is different under the two types of crawling gaits. In this paper, robotic efficiency was measured based on the robotic moving speed. Displacement was measured by using a laser displacement sensor (CD22-100VM12, FASTUS Inc., Japan), and the measuring error was 0.01 mm. The main parameters of the various parts of the spherical robot are shown in Table 2. Using Gait 2, the robot crawled 14 mm in approximate 95 s, whereas Gait 1 required a longer time. The results showed that the control of Gait 2 was relatively simple, and the moving speed was large. Controlling Gait 1 was more complex than controlling Gait 2, Gait 1 was suitable for crossing obstacles. The crawling speed of the robotic gait was not large—Gait 2 was 0.147 mm/s, and Gait 1 was 0.133 mm/s, which was probably because the SMA springs required long cooling time even in the presence of biased springs. Thus, we concluded that improving the cooling rate of SMA springs can improve the performance of SMA actuators. The robot's self-control ability is limited to being controlled by an open loop, therefore, it is necessary to consider autonomous motion controls in the future.

Table 2 Main parameters of various parts of the spherical robot

Parameter	Value	Unit
Weight of the robot	1095.2	g
Weight of the electromagnet	26	g
Weight of the SMA spring	1.47	g
Weight of one foot	66.07	g
Power of the electromagnet	24.5	N
Weight of hemispherical shell	155.7	g
Diameter of the shell	200	mm
Geometric parameters of the foot	110×34×20	mm

4.3 Ball motion model

As described earlier, the variable-model robot has the advantage of moving on slopes, and the speed of rolling depends on the angle of the flat surface. However, it is necessary to plan special gaits for the robot to roll on the lower slope. The rolling gait is shown in Figure 12(a), the colors shown in the picture are the same as those mentioned in Section 3.2. Figure 12(c) shows the robotic effect of rolling in the experiment. The marks A_1 and A_2 represent the outer springs of the foot, A_{11} and A_{22} are the inner springs of the foot. When A_1 and A_2 are heated, the robotic feet bend

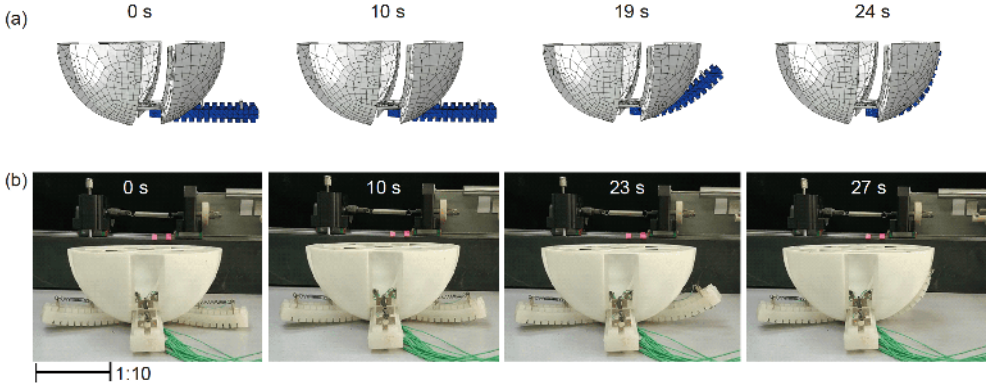

Figure 10 (Color online) Simulation and bending experiment. (a) Simulation; (b) bending experiment.

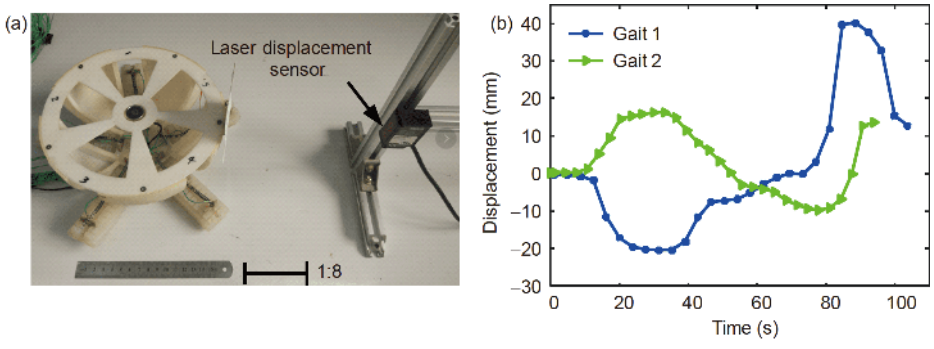

Figure 11 (Color online) Displacement of movement.

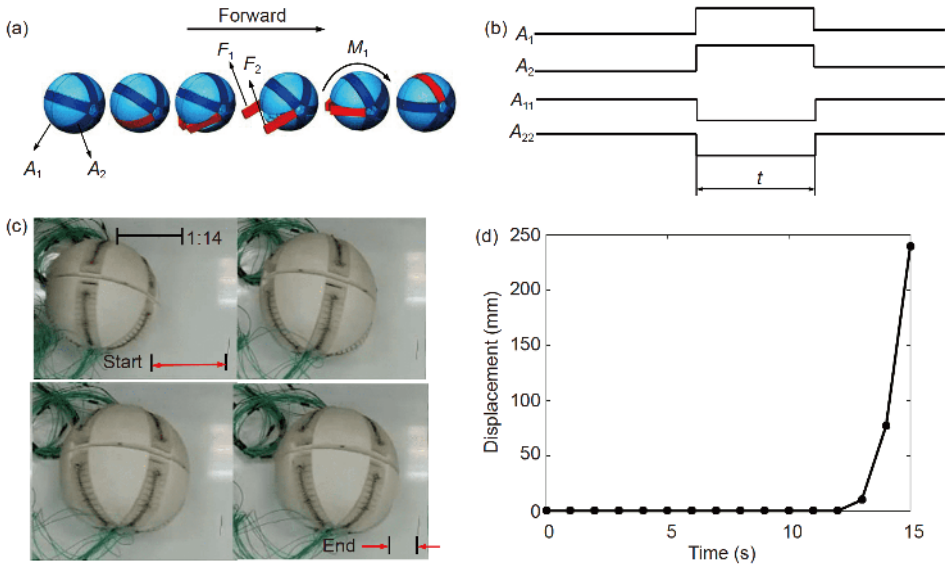

Figure 12 (Color online) Design for robotic rolling. (a) Heating strategy of the SMA springs for rolling; (b) heating strategy for the rolling gait; (c) rolling in the experiment; (d) rolling displacement on the slope with 0.022π.

outwards under the action of the spring force. At the same time, the ground exerts forces F_1 and F_2 on the feet, which produce the rolling torque M_1 for the robotic shell. Thus, the robot can achieve rolling by the torque M_1. After many experiments, we found that rolling on a plane is very difficult for the robot because the surface of the robot is not a standard arc. For rolling, it is necessary to overcome the friction between the shell and the slope. However, the robot can roll quickly on a flat surface at an angle of 0.022π, and the rolling process can be seen in the video of rolling.

4.4 Robotic movement test

4.4.1 Avoiding an obstacle

In Figure 13, the robot bypassed the obstacle with a size of 130 mm×95 mm×50 mm for about 1 h. The moving speed was not impressive, this was probably because the surface of the experimental platform was very smooth and the platform's friction coefficient was 0.5. In addition, the heating and cooling processes of the SMA springs were also important factors determining the moving speed. The robot did not have the ability of sensing; therefore, external control was necessary to bypass the obstacle. In the future, we propose to add multiple sensing modules, such as vision radar systems and temperature modules.

4.4.2 Flipping the obstacle

When the robot passed through the obstacle having a size of 150 mm×38 mm×22 mm, the robotic speed was slow at first, however, once the center of the gravity of the robot crossed the center of the obstacle, the robot could change its own center of gravity by bending its feet as shown in Figure 14(a).

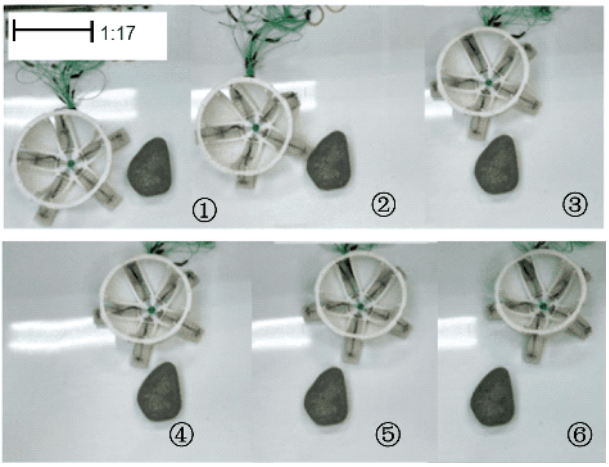

Figure 13 (Color online) Bypassing an obstacle.

In particular, the robot could roll on the surface of an obstacle with its shell when the robot's center of gravity was on the obstacle. This behavior can improve the robotic crossing speed.

4.4.3 Isolated sphere

As shown in Figure 14(b), when the robotic shell was separated, the middle layer of the spherical robot was perpendicular to the ground, and the sphere could be separated by turning on the electromagnetic switch. After being separated, the robot could enter a small space and simultaneously move in two directions. Currently, the robot lacks the ability to return to its original unseparated form because of the special structure of the robot. In our future research, we will focus on designing a robot having the ability to return to its spherical shape after separation.

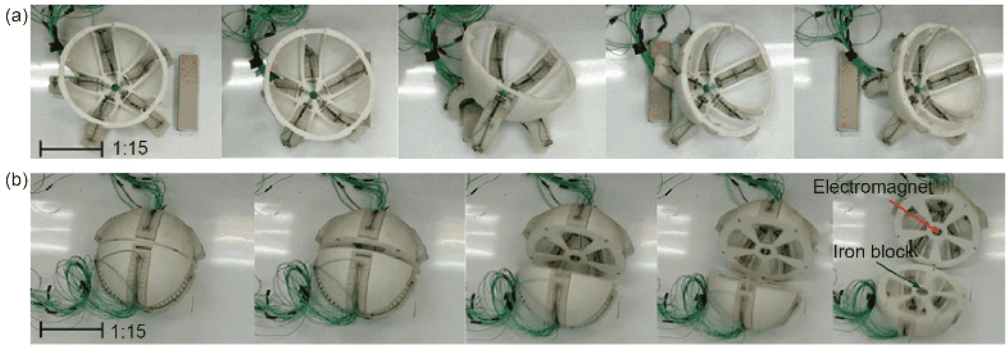

Figure 14 (Color online) (a) Crossing obstacles; (b) shell separation.

4.4.4 *Load capacity*

Weights of 550, 650, 750 and 850 g were fixed on the hemispherical body of the robot, and a load gait was used to drive the robot. The experimental results are shown in Figure 15. The robot's moving speed gradually decreased when the load weight increased, and the maximum load value was approximately 850 g. Current surveys show that most soft robots do not have this load capacity. At present, the weight values of most sensors are less than the load values used in this experiment. Therefore, this robot can carry multiple sensors to complete the specific tasks.

5 Conclusions

We fabricated a variable-model robot based on the bionic concept. The soft foot of the robot was made from silicone gel and was similar to the muscles of a starfish. SMA springs were used as robotic actuators. Based on the variations in the length of the SMA springs during heating, the special structure of the soft foot contained silicone and SMA springs. The experimental results demonstrated that the SMA springs could drive the foot to achieve a larger bending range response with a DC voltage of 3.8 V. This robot could achieve several basic movements using different gaits. In a smooth environment, the crawling cycle was approximately 105 s, and the load crawling cycle was approximately 95 s. The robot could carry a maximum load of approximately 850 g. The robot could climb over an obstacle having the size of 130 mm×95 mm×50 mm although it took nearly 1 h to do this. By adopting a spherical shape, the robot could roll fast on a slope and separate into two parts using a special control strategy. These results illustrated that this robot had multiple functions related to crawling, loading, rolling, and avoiding obstacles. The robot could achieve safe man-machine interactions and caused less damage to the environment. Therefore, it can function in a variety of environments.

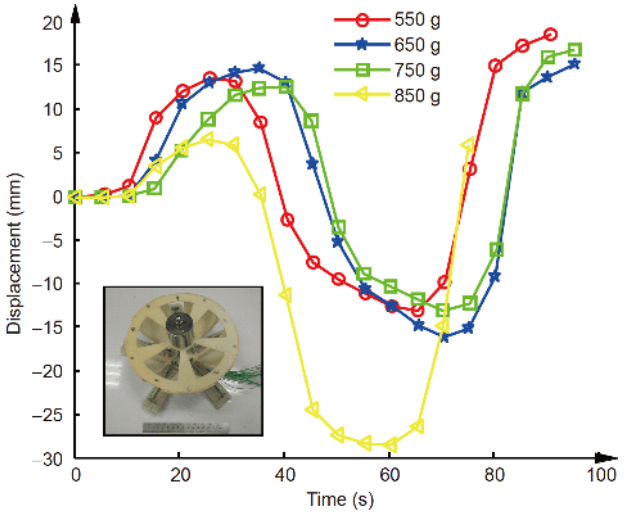

Figure 15 (Color online) Load capacity of the robot.

For the lag effect of the SMA spring in the experiment, we need to improve the cooling speed of SMA in our future research. At present, the control and power circuit are outside the robot, so the movement range is limited. In future, we propose to equip the robot with a power and a controller inside the body, which would be useful for reconnaissance missions.

This work was supported by the National Natural Science Foundation of China (Grant No. 61603015).

1 Zhong G, Chen L, Jiao Z, et al. Locomotion control and gait planning of a novel hexapod robot using biomimetic neurons. IEEE Trans Contr Syst Technol, 2018, 26: 624–636
2 Shin S R, Migliori B, Miccoli B, et al. Electrically driven micro-engineered bioinspired soft robots. Adv Mater, 2018, 30: 1704189
3 Zhang F, Li T, Luo Y. A new low moduli dielectric elastomer nano-structured composite with high permittivity exhibiting large actuation strain induced by low electric field. Compos Sci Tech, 2018, 156: 151–157
4 Zeng H, Wani O M, Wasylczyk P, et al. Light-driven, Caterpillar-inspired miniature inching robot. Macromol Rapid Commun, 2018, 39: 1700224
5 Henke E F M, Schlatter S, Anderson I A. Soft dielectric elastomer oscillators driving bioinspired robots. Soft Robotic, 2017, 4: 353–366

6 Jin H, Dong E, Xu M, et al. Soft and smart modular structures actuated by shape memory alloy (SMA) wires as tentacles of soft robots. Smart Mater Struct, 2016, 25: 085026
7 Martinez R V, Glavan A C, Keplinger C, et al. Soft actuators and robots that are resistant to mechanical damage. Adv Funct Mater, 2014, 24: 3003–3010
8 Cianchetti M, Arienti A, Follador M, et al. Design concept and validation of a robotic arm inspired by the octopus. Mater Sci Eng-C, 2011, 31: 1230–1239
9 Shepherd R F, Ilievski F, Choi W, et al. Multigait soft robot. Proc Natl Acad Sci USA, 2011, 108: 20400–20403
10 McMahan W, Chitrakaran V, Csencsits M, et al. Field trials and testing of the OctArm continuum manipulator. In: Proceedings 2006 IEEE International Conference on Robotics and Automation. Orlando: IEEE, 2006. 2336–2341
11 Kim H I, Han M W, Song S H, et al. Soft morphing hand driven by SMA tendon wire. Compos Part B-Eng, 2016, 105: 138–148
12 Li Z, Du R. Design and analysis of a bio-inspired wire-driven multisection flexible robot. Int J Adv Robotic Syst, 2013, 10: 209–220
13 Rolf M, Steil J J. Constant curvature continuum kinematics as fast approximate model for the Bionic Handling Assistant. In: 2012 IEEE/RSJ International Conference on Intelligent Robots and Systems. Vilamoura: IEEE, 2012. 3440–3446
14 Lei J, Yu H, Wang T. Dynamic bending of bionic flexible body driven by pneumatic artificial muscles (PAMs) for spinning gait of quadruped robot. Chin J Mech Eng, 2016, 29: 11–20
15 Sun Q P, Aslan A, Li M P, et al. Effects of grain size on phase transition behavior of nanocrystalline shape memory alloys. Sci China Tech Sci, 2014, 57: 671–679
16 Rodrigue H, Wang W, Kim D R, et al. Curved shape memory alloy-based soft actuators and application to soft gripper. Compos Struct, 2017, 176: 398–406
17 Roh J H, Kim J S, Kwon O H. Vibration behaviors of hybrid smart composites with SMA strips reinforced SMP lamina under blast loading. Compos Struct, 2015, 125: 417–424
18 Shen Q, Trabia S, Stalbaum T, et al. A multiple-shape memory polymer-metal composite actuator capable of programmable control, creating complex 3D motion of bending, twisting, and oscillation. Sci Rep, 2016, 6: 24462
19 Guo C, Chunya W U, Liu H. Application progress of ionic polymer-metal composites actuator in robots. J Mech E, 2017, 53: 001
20 Henke E F M, Wilson K, Anderson I. Modeling of dielectric elastomer oscillators for soft biomimetic applications. Bioinspir Biomim, 2018, 13: 046009
21 Shintake J, Rosset S, Schubert B, et al. Versatile soft grippers with intrinsic electroadhesion based on multifunctional polymer actuators. Adv Mater, 2016, 28: 231–238
22 Trivedi D, Rahn C D, Kier W M, et al. Soft robotics: Biological inspiration, state of the art, and future research. Appl BIon Biomech, 2014, 5: 99–117
23 Wu J, Yu G, Gao Y, et al. Mechatronics modeling and vibration analysis of a 2-DOF parallel manipulator in a 5-DOF hybrid machine tool. Mech Mach Theory, 2018, 121: 430–445
24 Wu J, Wang J, Wang L, et al. Dynamics and control of a planar 3-DOF parallel manipulator with actuation redundancy. Mech Mach Theory, 2009, 44: 835–849
25 Kim S, Laschi C, Trimmer B. Soft robotics: A bioinspired evolution in robotics. Trends Biotech, 2013, 31: 287–294
26 Wu J, Wang J, You Z. An overview of dynamic parameter identification of robots. Robot Comput Integr Manuf, 2010, 26: 414–419
27 Roche E T, Wohlfarth R, Overvelde J T B, et al. Actuators: A bioinspired soft actuated material (Adv. Mater. 8/2014). Adv Mater, 2014, 26: 1145
28 Rodrigue H, Wang W, Han M W, et al. An overview of shape memory alloy-coupled actuators and robots. Soft Robotic, 2017, 4: 3–15
29 Kim Y, Desai J P. Design and kinematic analysis of a neurosurgical spring-based continuum robot using SMA spring actuators. In: 2015 IEEE/RSJ International Conference on Intelligent Robots and Systems. Hamburg: IEEE, 2015. 1428–1433
30 Wang L, Liu J. Compatible hybrid 3D printing of metal and nonmetal inks for direct manufacture of end functional devices. Sci China Tech Sci, 2014, 57: 2089–2095
31 Mao S, Dong E, Xu M, et al. Design and development of starfish-like robot: Soft bionic platform with multi-motion using SMA actuators. In: 2013 IEEE International Conference on Robotics and Biomimetics. Shenzhen: IEEE, 2013. 91–96